Editors' Suggestion

Physical Observation of a Robust Acoustic Pumping in Waveguides with Dynamic Boundary

Xianchen Xu,[1,*] Qian Wu,[1,*] Hui Chen,[1,*] Hussein Nassar,[1] Yangyang Chen,[1] Andrew Norris,[2] Michael R. Haberman,[3] and Guoliang Huang[1,†]

[1]Department of Mechanical and Aerospace Engineering, University of Missouri, Columbia, Missouri 65211, USA
[2]Mechanical and Aerospace Engineering, Rutgers University, Piscataway, New Jersey 08854-8058, USA
[3]Walker Department of Mechanical Engineering and Applied Research Laboratories, The University of Texas at Austin, Austin, Texas 78712, USA

(Received 29 June 2020; accepted 11 November 2020; published 15 December 2020)

Research on breaking time-reversal symmetry to realize one-way wave propagation is a growing area in photonic and phononic crystals and metamaterials. In this Letter, we present physical realization of an acoustic waveguide with spatiotemporally modulated boundary conditions to realize nonreciprocal transport and acoustic topological pumping. The modulated waveguide inspired by a water wheel consists of a helical tube rotating around a slotted tube at a controllable speed. The rotation of the helical tube creates moving boundary conditions for the exposed waveguide sections at a constant speed. We experimentally demonstrate acoustic nonreciprocity and topologically robust bulk-edge correspondences for this system, which is in good agreement with analytical and numerical predictions. The nonreciprocal waveguide is a one-dimensional analog to the two-dimensional quantum Hall effect for acoustic circulators and is characterized by a robust integer-valued Chern number. These findings provide insight into practical implications of topological modes in acoustics and the implementation of higher-dimensional topological acoustics where time serves as a synthetic dimension.

DOI: 10.1103/PhysRevLett.125.253901

The law of reciprocity is a fundamental principle and design constraint of waves and vibrations control in linear, time-invariant systems that require energy transport between two points in space to be symmetric. Thus, reciprocity can be a hindrance in systems where asymmetric wave motion is sought. For example, one-way acoustic devices, such as three-port circulators [1] and one-way diodes [2], cannot exist with unbroken reciprocity [3–8]. Creating nonreciprocal materials and devices has therefore attracted tremendous attention for enabling unidirectional energy transport [9–17], topological insulators [18,19], and edge modes [20,21]. Many strategies, including strongly nonlinear networks [22–26], gyroscopic media [27,28], circulating fluids [29,30], and spatiotemporally modulated materials [31–39], have been proposed. Among them, spatiotemporal modulation by introducing a temporal topological pumping has been widely investigated in active elastodynamic systems. However, the physical realization of the temporal pumping generally requires sophisticated external fields or smart materials applied in the system. For example, nonreciprocity induced by electromechanical pumping was recently experimentally demonstrated by introducing a periodic array of electromagnets on a beam to control positive and negative propagating mechanical waves [31]. A similar approach was adopted experimentally by proposing a magnetomechanical topological insulator to demonstrate the temporal pumping that produces robust mechanical energy transport [38]. Surprisingly, compared with their mechanical counterparts, there are few works on physical evidence of spatiotemporal pumping in acoustics, not to mention the nonreciprocal and topological transport of acoustic waves.

In this Letter, we propose a 1D dynamic waveguide that displays nonreciprocal wave phenomena without imposing external fields to modulate the acoustic properties in space and time. Rather, we employ a novel paradigm whereby the bulk properties are left intact, while the boundary conditions are, through purely mechanical means, modulated in space and time. This is achieved by mounting a helical tube on a slotted acoustic waveguide and then rotating the helix with a motor, as shown in Fig. 1(a). This configuration is shown to be capable of pumping acoustic energy unidirectionally in a manner reminiscent of a water wheel. The system results in an acoustic waveguide with exposed holes (shunts) that are effectively translated at a constant speed along the axis of the waveguide when the helical tube is rotated by the motor. It is worth noting that, while the properties of the tube are time independent, the boundary conditions and therefore the impedance of the waveguide is indeed time dependent, leading to the "dynamic" waveguide [31]. This strategy differs from the acoustic pumping where wavelike modulations of constitutive parameters are utilized to study parametric amplification in the unstable regime [40]. As a result, the modulated acoustic waveguide

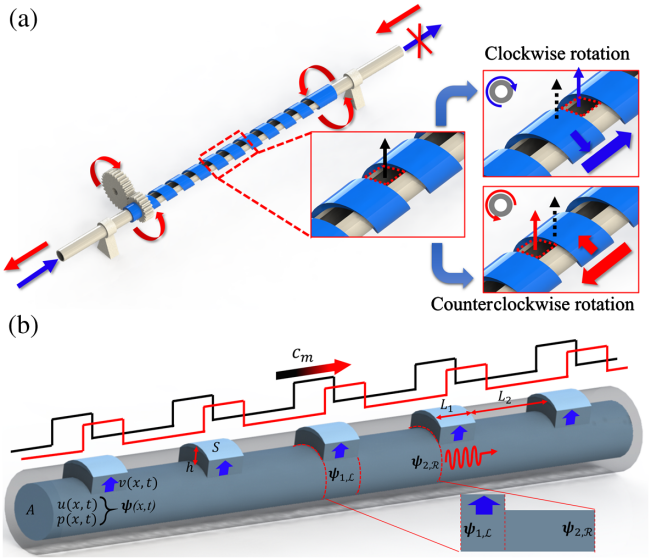

FIG. 1. (a) Schematic illustration of the modulated acoustic waveguide. A fixed, slotted tube (gray) with a long straight opening is inserted into a helical tube (blue), forming an array of parallelogram openings in the acoustic waveguide. The helical tube is driven mechanically by a motor system. Clockwise and counterclockwise rotations realize forward and backward spatiotemporal modulation, respectively, as the exposed sections translate, indicated by the insets. (b) Schematic of the equivalent spatiotemporally modulated medium. The gray and light blue regions represent the rigid material and air, respectively. The moving exposed sections enable the spatiotemporal modulation of waveguide boundary conditions. $p(x,t)$ and $u(x,t)$ represent the longitudinal pressure and velocity fields in the tube, "$\mathcal{R}$" and "$\mathcal{L}$" denote the right and left interfaces of the unit cell, respectively.

supports nonreciprocal acoustic energy transport and acoustic topological pumping. We experimentally demonstrate the nonreciprocal acoustic wave propagation when the modulation speed is small compared to the sound speed in the waveguide and that the frequency range of nonreciprocity can be tuned by changing the angular velocity of the helix. We further experimentally illustrate the acoustic topological bulk-edge correspondence under different boundary conditions. The experimental results are in good agreement with analytical predictions and numerical simulations.

Theoretical predictions of wave behavior in the proposed system are conducted by modeling the acoustic tube with moving, exposed sections (ESs) as a two-phase medium with translating phases, as shown in Fig. 1(b). Rotation of the helical tube results in a linear speed c_m of the ESs relative to the acoustic waveguide reference frame. The boundary condition of the acoustic waveguide is hence time dependent with a nonzero modulation speed $c_m = \omega_m/k_m$. In this scenario, the air column moves in and out through the ESs at a modulated vertical velocity $v(x,t) = V\{1+\exp[-\mu\cos(\omega_m t - k_m x) - \mu\cos(\pi\gamma)]\}^{-1}$, driven by the pressure $p(x,t)$ in the ESs according to Newton's law $p(x,t)S = M\partial_t v(x,t)$ [41]. Here $\mu = 5$ is chosen, which does not necessarily influence the numerical results but optimizes the numerical convergence (Supplemental Material [42], Sec. A). The ES acts as a sink that modifies the equations of motion in the ES,

$$-\left(\frac{1}{B}\right)\partial_t p(x,t) = \partial_x u(x,t) + \left(\frac{\sigma_1}{A}\right)v(x,t), \quad (1)$$

$$-\partial_x p(x,t) = \rho\partial_t u(x,t), \quad (2)$$

where A denotes the tube cross-sectional area, B and ρ are the bulk modulus and density of air, respectively, $\sigma_1 = NS$ with $N = (L_1+L_2)^{-1}$, and $M = \rho Sh$. While for the nonexposed section, the general equations of motion read

$$-\left(\frac{1}{B}\right)\partial_t p(x,t) = \partial_x u(x,t), \quad (3)$$

$$-\partial_x p(x,t) = \rho\partial_t u(x,t). \quad (4)$$

We utilize the transfer matrix method to visit the acoustic nonreciprocal regime for various modulation speeds c_m (see Supplemental Material [42], Sec. A for derivation details). The effect of slow modulations (the modulation frequency is smaller than the bandwidth) is to shear the dispersion curves and create a couple of directional band gaps. The emergence of the direction gaps is the direct observation of the band-tilting-induced nonreciprocity.

Progressive modulation in various modulation frequency regions creates a bias in space and time, which enables nonreciprocal wave propagation as a function of modulation frequency and depth. For a small modulation speed, the phase shift induced by adiabatic pumping over a short time period is insufficient to trigger any intermodal transitions and the band structure gets sheared and tilted to create a directional band gap [8,43]. For a small-amplitude and moderate modulation speed, Bragg scattering due to time-dependent interface causes the frequency shift for scattered waves, which is related to Doppler shifting [45]. Figure 2(a) illustrates the theoretical dispersion relations of the modulated waveguide with a small modulation speed $c_m = 0.029c_0$, where the modulation frequency ($\omega_m = 20$ rad/s) is much smaller than the width of the first band gap ($\delta\omega = 160$ rad/s). In this example, the geometric parameters are $L_1 = 0.01$ m, $L_2 = 0.03$ m, $S = L_1^2 = 1\times10^{-4}$ m^2, $\sigma_1 = 0.25\times10^{-2}$ m, and $A = 1.54\times10^{-4}$ m^2. The air density, bulk modulus, and mass of air in the exposed sections are $\rho = 1.21$ kg m^{-3}, $B = 1.42\times10^5$ Pa, and $M = 1.21\times10^{-7}$kg, respectively. In Fig. 2(a), we notice that the lower boundary at $kL = 0$ does not shift, indicating that the first cutoff frequency is independent of the modulation speed. This is because the first cutoff frequency

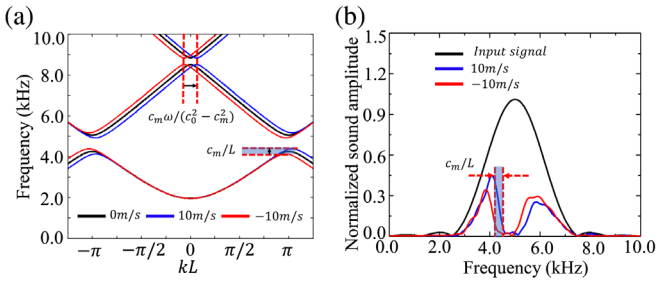

FIG. 2. (a) Analytically calculated dispersion diagrams of the modulated effective medium with $c_m = 10$ (solid blue), 0 (solid black), and -10 m/s (solid red). A frequency shift of the band gap lower bound $\Delta f = c_m/L$ is obtained when modulated from $c_m = 10$ to $c_m = -10$ m/s. (b) Normalized sound amplitudes from numerical simulations for modulation speeds $c_m = 10$ (solid blue) and $c_m = -10$ m/s (solid red). The solid black curve represents the input signal.

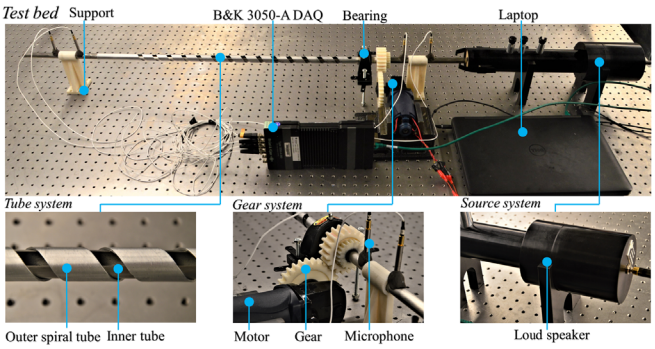

FIG. 3. Experimental setup of the spatiotemporal modulated acoustic system. The test bed is composed of three main components: a tube system composed of the slotted tube and exposed helical tube, a gear system and motor to drive the rotation of the outer helical tube, and an acoustic testing system containing a loudspeaker and four acoustic transducers (probes).

corresponds to a stationary wave at $k = 0$ and therefore is insensitive to the modulation when the modulation speed is slow. The effect of the modulation speed on the cutoff frequency has been investigated in detail [43]. However, its upper boundary exhibits a frequency shift of c_m/L. Accordingly, the band gaps become directional, resulting in nonreciprocal wave propagation at these frequencies. Frequency shifts of the second and third passbands are also observed. The continuous modulation-induced tilting of the dispersion curves can be interpreted by the adiabatic theorem for slow modulation. The frequency shift is determined by $C\omega_m$, where C is the Chern number (Supplemental Material [42], Sec. B). To validate the theoretical prediction, numerical simulations for the modulated system (Fig. 1) are conducted using a finite-element method (FEM)-based software COMSOL Multiphysics. In the simulations, a five-cycle tone burst signal $p = [1 - \cos(0.5\pi f_c t)]\sin(2\pi f_c t)$ centered at $f_c = 5$ kHz is applied at one end of the tube and the time-domain transmitted signal is measured at the other end. Based on Fourier transform, Fig. 2(b) illustrates the frequency spectra of the incidence and transmission with $c_m = 10$ m/s and without modulation. To reduce the undesired reflection, time-domain perfect matching layers are applied on both ends of the tube (Supplemental Material [42], Sec. C). As shown in Fig. 2, the acoustic nonreciprocity is observed around the lower and upper boundaries of the first stop band, shifting the first branch up to c_m/L compared with the nonmodulated case. A possible realistic experimental setup and the associated measuring procedure are discussed in Sec. C of the Supplemental Material [42]. In addition, the acoustic wave propagation at other frequencies are tilted with transmitted amplitudes unaltered. The time-domain numerical results demonstrate that the acoustic pumping is sufficient to break reciprocity when traveling along the modulation direction and suppressed in the other direction.

We experimentally demonstrate the acoustic band-tilting-induced nonreciprocity using a purely mechanical test bed, as shown in Fig. 3. The test bed, fixed to a vibration isolation platform by 3D printed supports, is a full realization of the numerical model illustrated in Fig. 1. Both the slotted and helical tubes are made from aluminum. The inner slotted tube and outer helical tube have inner radii of 7 and 8.2 mm and outer radii of 8 and 9.3 mm, respectively. The helical tube is rotated by a motor. We used Mecanum's four microphone impedance tubes and collected the data with a B&K 3050-A data acquisition (DAQ) system. While the helical tube rotates, the ESs translate along the tube axis (see video in the Supplemental Material [42]). Acoustic signals are generated with a loudspeaker on the right side of the tube. Four acoustic transducers, working as probes, are placed to collect the reflected and transmitted signals (see Fig. 3). The contact areas of the two tubes are filled with lubricant to prevent sound leakage and reduce noise.

We first measured the sound transmission by translating the ESs characterized by moving boundary conditions. The loudspeaker is driven a by swept-sine input covering 1–5 kHz. When the rotation is sufficiently slow to satisfy the adiabatic condition, the bulk bands of the modulated tube are tilted with respect to their static reference configuration (see also Fig. 2). A directional band gap appears around 4450 Hz with a small modulation speed of $c_m = +10$ m/s. This enables the sound to transmit within the frequency range of 4450–$(4450 + c_m/2L)$ Hz, which is forbidden when the tube is static. In other words, nonreciprocal sound transport is triggered within the band gap when the tube is rotating; see Fig. 4(a). As expected, good agreement between numerical and experimental results is observed. The nonreciprocal frequency region is marked by the blue-shaded area in Fig. 4(a), where the clockwise (CW) and counterclockwise (CCW) modulations display asymmetric transmission with a bandwidth of

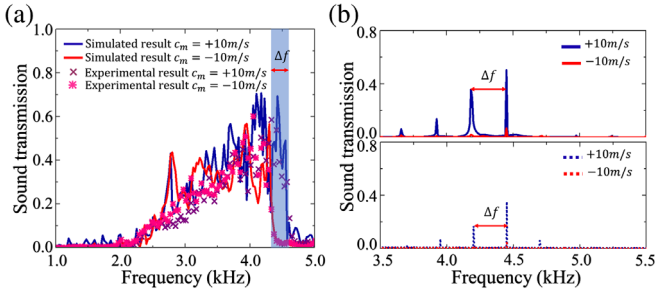

FIG. 4. Comparison of the sound transmission spectrum of the spatiotemporally modulated acoustic material. (a) Simulation results with modulation speeds $c_m = 10$ (solid blue) and $c_m = -10$ m/s (solid red), and the corresponding experimental results with modulation speeds $c_m = 10$ (purple cross) and $c_m = -10$ m/s (pink star). (b) Simulations (solid) and experiments (dotted) for modulation speeds $c_m = 10$ (blue) and $c_m = -10$ m/s (red) under the excitation at 4450 Hz.

$\Delta f = c_m/L$. To better quantify the nonreciprocal behavior, numerically and experimentally attained transmission spectra under harmonic loading at $f_e = 4450$ Hz is plotted in Fig. 4(b). The magnitudes of sound transmission at the excitation frequencies (within the modulation passband) are significantly greater than those for the negative modulation (within the modulation band gap). Moreover, the intensities of lower harmonics (in the passband) are much stronger than those of the higher ones (within the band gap). Further, high-order harmonics are observed as additional peaks, with multiple frequencies $f = f_e \pm n\Delta f$, where $\Delta f = 250$ Hz, and $n = 0, 1, 2, \ldots$. These extra harmonics are the consequence of the traveling waves being scattered by the moving boundaries as in the Doppler effect [6]. It should be mentioned that, in spite of the lossy characteristics of the ESs, the nonreciprocal behavior is still noticeable since it is quantized by a robust Chern number (Supplemental Material [42], Secs. B and C).

Topological pumping and band-tilting-induced nonreciprocity in our system have an identical underlying origin: both are characterized by the same Chern number. To examine the topological pumping, it is essential to quantify the acoustic mode shapes through a pumping cycle: it overcomes (or overrides) the band gap and enables the propagation of sound within it and, further, can be captured by a nonzero Chern number according to the principle of bulk-edge correspondence [46]. In the current design, we can assume that the CW rotation of the tube corresponds to the modulation of the ESs in the forward direction (0–20 mm). In this way, the CCW rotation automatically corresponds to the backward modulation (20–0 mm). Figure 5(a) shows the numerically calculated eigenfrequencies of a finite tube composed of 15 ESs with different edge position instants under fixed boundary conditions applied upon both ends (see Supplemental Material [42], Sec. C for more numerical details). As the helical tube rotates, the right and left edge modes, marked by the red and blue dots in Fig. 5(a), exist within the band gap. Within one modulation period, a transition from the bulk mode, to the right edge, then back to the bulk, and eventually to the left mode can be identified, exhibiting the adiabatic topological pumping process. The mode shapes of the (i) bulk mode, (ii) right edge mode, and (iii) left edge mode are correspondingly shown in Fig. 5(b) for demonstration purposes.

To observe the topological pumping, we conduct experiments by turning the tube under different boundary conditions to examine the bulk-edge correspondence principle through a pumping cycle (Supplemental Material [42], Sec. D). The test bed is identical to what has been shown in Fig. 3, except the helical tube is manually turned to certain position instants and remains static. A microphone with subwavelength dimension is placed inside the tube for scanning the pressure field distribution along the tube axis (Supplemental Material [42], Sec. D). Harmonic excitations of different frequencies are then applied when the phase of the modulated tube is swept over one complete rotation of 2π by manually translating the ESs from 0 to 20 mm (Supplemental Material [42], Sec. D). The measured pressure field distributions at three different position instants, corresponding to the three highlighted eigenmodes in Fig. 5(a), are presented in Fig. 5(b) by symbol plots. For the bulk mode around 4.4 kHz illustrated in Fig. 5(b)(i), except for the magnitude decrease due to sound attenuation, a standing wave profile is still observable describing the bulk mode. The right (under the left excitation) and left (under the right excitation) edge modes are shown in Fig. 5(b)(ii) and (iii), respectively. The establishment of the acoustic localization under the excitations on the opposite sides proves the existence of the

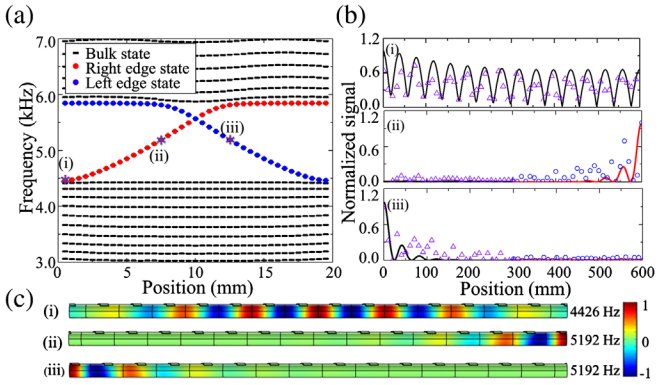

FIG. 5. (a) Evolution of eigenfrequencies of a finite tube (15 unit cells) over one period of modulation under fixed boundary condition. (b) Normalized acoustic pressure distributions at modes (i)–(iii) shown in (a). The black and red solid curves denote the simulation incident signals from the right and left sides, respectively. The purple triangular and blue circular dots represent the corresponding experimental measurements. (c) Mode shapes (pressure distribution) from FEM numerical simulations at modes (i)–(iii).

topological edge modes (Supplemental Material [42], Sec. D). Eigenfrequency analysis also provides the acoustic pressure distributions at these position instants (i)–(iii), as shown in Fig. 5(c). Good agreement with the measured normalized acoustic distributions is evidenced. Finally, to directly validate the localized edge mode, broadband acoustic harmonic tests are implemented by applying acoustic excitation on both the right and left sides of the system under phase condition (ii) (see Supplemental Material [42], Sec. D for the measured frequency spectrum of the edge mode). The results confirm the emergence of the topologically protected edge mode localized around the right end of the tube under the current phase condition.

In summary, we have experimentally demonstrated the mechanically modulation-induced nonreciprocity in acoustics and the adiabatic topological pumping phenomena, associated with the purely mechanical realization of spatiotemporally modulated acoustic waveguide. The spatiotemporal modulation behaving as an acoustic pumping strategy offers unprecedented control and reconfigurability over the acoustic energy transport in space and even in frequency dimensions. We believe that the proposed mechanical realization of the acoustic modulated nonreciprocal systems paves the way for realizing topological phononic logic and acoustic energy localization and trapping applications.

This work is supported by the Air Force Office of Scientific Research under Grants No. AF 9550-18-1-0342 and No. AF 9550-20-0279, the NSF EFRI under Grant No. 1641078, and the Army Research Office under Grant No. W911NF-18-1-0031.

*X. X., Q. W. and H. C. contributed equally to this work.
†huangg@missouri.edu

[1] R. Fleury, D. L. Sounas, C. F. Sieck, M. R. Haberman, and A. Alù, Science **343**, 516 (2014).
[2] N. Boechler, G. Theocharis, and C. Daraio, Nat. Mater. **10**, 665 (2011).
[3] S. Zhang, L. Yin, and N. Fang, Phys. Rev. Lett. **102**, 194301 (2009).
[4] J. Zhu, J. Christensen, J. Jung, L. Martin-Moreno, X. Yin, L. Fok, X. Zhang, and F. J. Garcia-Vidal, Nat. Phys. **7**, 52 (2011).
[5] T. Brunet, A. Merlin, B. Mascaro, K. Zimny, J. Leng, O. Poncelet, C. Aristégui, and O. Mondain-Monval, Nat. Mater. **14**, 384 (2015).
[6] B. Liang, X. S. Guo, J. Tu, D. Zhang, and J. C. Cheng, Nat. Mater. **9**, 989 (2010).
[7] H. Nassar, H. Chen, A. N. Norris, and G. L. Huang, Phys. Rev. B **97**, 014305 (2018).
[8] H. Nassar, B. Yousefzadeh, R. Fleury, M. Ruzzene, A. Alù, C. Daraio, A. N. Norris, G. Huang, and M. R. Haberman, Nat. Rev. Mater. **5**, 667 (2020).
[9] D. Jalas, A. Petrov, M. Eich, W. Freude, S. Fan, Z. Yu, R. Baets, M. Popović, A. Melloni, J. D. Joannopoulos, and M. Vanwolleghem, Nat. Photonics **7**, 579 (2013).
[10] L. Lin, P. Hu, J. Shi, C. M. Appleton, K. Maslov, L. Li, R. Zhang, and L. V. Wang, Nat. Commun. **9**, 2352 (2018).
[11] H. S. Park and B. K. Oh, J. Sound Vib. **418**, 122 (2018).
[12] J. W. Strutt, Proc. London Math. Soc. **s1–4**, 357 (1871).
[13] J. A. Achenbach and J. D. Achenbach, *Reciprocity in Elastodynamics* (Cambridge University Press, Cambridge, England, 2003).
[14] M. R. Haberman and M. D. Guild, Phys. Today **69**, No. 6, 42 (2016).
[15] S. A. Cummer, J. Christensen, and A. Alù, Nat. Rev. Mater. **1**, 16001 (2016).
[16] Y. Zheng, Z. Wu, X. Zhang, and K. W. Wang, Smart Mater. Struct. **28**, 045005 (2019).
[17] B. Yuan, B. Liang, J. C. Tao, X. Y. Zou, and J. C. Cheng, Appl. Phys. Lett. **101**, 043503 (2012).
[18] A. B. Khanikaev, S. H. Mousavi, W. K. Tse, M. Kargarian, A. H. MacDonald, and G. Shvets, Nat. Mater. **12**, 233 (2013).
[19] Z. Zhang, Q. Wei, Y. Cheng, T. Zhang, D. Wu, and X. Liu, Phys. Rev. Lett. **118**, 084303 (2017).
[20] L. M. Nash, D. Kleckner, A. Read, V. Vitelli, A. M. Turner, and W. T. Irvine, Proc. Natl. Acad. Sci. U.S.A. **112**, 14495 (2015).
[21] D. J. Apigo, W. Cheng, K. F. Dobiszewski, E. Prodan, and C. Prodan, Phys. Rev. Lett. **122**, 095501 (2019).
[22] M. Maldovan. Nature (London) **503**, 209 (2013).
[23] C. Liu, Z. Du, Z. Sun, H. Gao, and X. Guo, Phys. Rev. Applied **3**, 064014 (2015).
[24] Z. Zhang, I. Koroleva, L. I. Manevitch, L. A. Bergman, and A. F. Vakakis, Phys. Rev. E **94**, 032214 (2016).
[25] B. I. Popa and S. A. Cummer, Nat. Commun. **5**, 3398 (2014).
[26] B. Liang, B. Yuan, and J. C. Cheng, Phys. Rev. Lett. **103**, 104301 (2009).
[27] P. Wang, L. Lu, and K. Bertoldi, Phys. Rev. Lett. **115**, 104302 (2015).
[28] M. Garau, M. J. Nieves, G. Carta, and M. Brun, Int. J. Eng. Sci. **143**, 115 (2019).
[29] R. Fleury, D. L. Sounas, and A. Alù, Phys. Rev. B **91**, 174306 (2015).
[30] Y. G. Peng, C. Z. Qin, D. G. Zhao, Y. X. Shen, X. Y. Xu, M. Bao, H. Jia, and X. F. Zhu, Nat. Commun. **7**, 13368 (2016).
[31] Y. Wang, B. Yousefzadeh, H. Chen, H. Nassar, G. Huang, and C. Daraio, Phys. Rev. Lett. **121**, 194301 (2018).
[32] Y. Chen, X. Li, H. Nassar, A. N. Norris, C. Daraio, and G. Huang, Phys. Rev. Applied **11**, 064052 (2019).
[33] C. Shen, X. Zhu, J. Li, and S. A. Cummer, Phys. Rev. B **100**, 054302 (2019).
[34] J. Li, C. Shen, X. Zhu, Y. Xie, and S. A. Cummer, Phys. Rev. B **99**, 144311 (2019).
[35] A. Baz, J. Acoust. Soc. Am. **143**, 1376 (2018).
[36] S. P. Wallen and M. R. Haberman, Phys. Rev. E **99**, 013001 (2019).
[37] B. M. Goldsberry, S. P. Wallen, and M. R. Haberman, J. Acoust. Soc. Am. **146**, 782 (2019).
[38] I. H. Grinberg, M. Lin, C. Harris, W. A. Benalcazar, C. W. Peterson, T. L. Hughes, and G. Bahl. Nat. Commun. **11**, 974 (2020).
[39] Q. Wu, H. Chen, H. Nassar, and G. L. Huang, J. Mech. Phys. Solids **146**, 104196 (2020).

[40] A. A. Oliner and A. Hessel, IEEE Trans. Microwave Theory Tech **9**, 337 (1961).
[41] S. H. Lee, C. M. Park, Y. M. Seo, Z. G. Wang, and C. K. Kim, J. Phys. Condens. Matter **21**, 175704 (2009).
[42] See Supplemental Material at http://link.aps.org/supplemental/10.1103/PhysRevLett.125.253901 for more details on analytical modeling of the modulated acoustic tube with exposed sections, topological pumping and Chern number, and simulation and experimental methods, which includes Refs. [7,41,43,44].
[43] H. Nassar, X. C. Xu, A. N. Norris, and G. L. Huang, J. Mech. Phys. Solids **101**, 10 (2017).
[44] T. Fukui, Y. Hatsugai, and H. Suzuki, J. Phys. Soc. Jpn. **74**, 1674 (2005).
[45] G. M. Gibson, E. Toninelli, S. A. Horsley, G. C. Spalding, E. Hendry, D. B. Phillips, and M. J. Padgett, Proc. Natl. Acad. Sci. U.S.A. **115**, 3800 (2018).
[46] H. Chen, L. Y. Yao, H. Nassar, and G. L. Huang, Phys. Rev. Appl. **11**, 044029 (2019).